

<https://doi.org/10.1038/s41699-025-00564-2>

# Unveiling inverse piezoelectricity and field induced nonvolatile strain in 2D TMDs



Utpreksh Patbhaje , Rupali Verma, Jeevesh Kumar, A Ansh & Mayank Shrivastava

The advancement of transition metal dichalcogenide (TMD)-based electronics technology demands thorough understanding of dominant electrical instability mechanisms. Through rigorous analysis, we identify a previously unrecognized non-volatile strain in TMDs that emerges during electrical operation, distinct from known instability mechanisms. Strain induced by electrical operation in TMD devices distinctly impacts electron and hole transport, as evidenced by the performance evolution of our ambipolar MoSe<sub>2</sub> field effect transistors (FETs). Raman spectroscopy, photoluminescence, and work function measurements reveal tensile strain in the channel and compressive strain near the contacts. This strain mismatch between the channel and contact regions disrupts charge transport and leads to instability in electrical performance. These instabilities are inevitable as they originate from the interaction between the electric field and the piezoelectric properties of TMDs and are expected to intensify in the field-accelerated downscaled devices. If unaddressed, these instabilities could severely limit the practical and commercial viability of TMD-based electronics.

2D materials such as the transition metal dichalcogenides (TMDs) are layered semiconducting materials predicted to replace or complement conventional materials, owing to their superlative properties, in the post-Moore era for nanoelectronics, optoelectronic, and quantum devices and systems<sup>1,2</sup>. However, these novel materials have not achieved their predicted potential yet, rooted to several material and interface anomalies that lead to bottleneck in their commercial adoption. In the initial works, reasons for unreliable performance in these TMD field effect transistors (FETs) were mostly attributed to traps originating from the gate and substrate oxide, processing and ambient induced defects<sup>3–11</sup>. The devices were stressed at lower fields and for shorter times in most reports. These reports had comprehensive findings that led to significant advances in the processing steps of the devices and control of measurement conditions to alleviate some common reliability concerns. The effect of applied electrical stress on the TMD material in channel itself was not satisfactorily discussed. Very recent reports demonstrated MoS<sub>2</sub> channel reformation under the moderate to high electric field operation leading to question the stability of TMD as channel material under considerable electrical fields. Such electrical stresses led to performance degradation and eventual time-dependent breakdown when stressed for longer times<sup>12–16</sup>. Performance instability and drifts due to channel degradation are going to remain as one of the major hurdles while getting TMDs to an acceptable commercial state.

All the prior reports emphasized addressing and accounting the intrinsic properties of TMDs to build a robust technology platform, while the universal picture and the root cause analysis might be still missing some aspects recognized in the reports. In the present and upcoming era of TMD

devices, exposure to high fields and high currents is inevitable. For example, recently reported ultra-high drive currents in the short channel (~100 nm) 2D TMD-based FETs exceeding international roadmap for devices and systems (IRDS) requirements were demonstrated to function at very high lateral fields (0.01 MV/cm to 0.4 MV/cm)<sup>17–23</sup>. It becomes very important to account for the impact of piezoelectric properties of a TMD crystal when devices operate at such high fields for accurate understanding of its implications on the TMD based devices.

To build the universal picture and probe the root cause of reliability issues, we usually associate the performance drifts and channel reconfigurations to a fundamental property of TMD and constituents of the FETs. A very important material property in the case of TMDs which has not been accounted for in prior work is its appreciable inverse piezoelectric response. Piezoelectric response to the applied electric fields leads to the accumulation of strain in devices. The resulting strain is governed by the piezoelectric tensor responding to the applied field vector which has directionality associated<sup>24,25</sup>. If the resulting strain was self-relaxing, then the channel performance wouldn't drift as a function of time as soon as the applied field is removed. However, we report the strain to cause runtime changes in material properties leading to FET performance instabilities. We test and validate this hypothesis in this work and reveal a potential fundamental showstopper for TMDs.

We chose MoSe<sub>2</sub> as it has the highest reported piezoelectric coefficients among the popularly used TMDs. We used advanced spectroscopic and mapping techniques to thoroughly examine the intricate interplay between material properties and device performance under varying stress conditions.

This work not only aims to deepen the understanding of the TMD's attributes causing these performance drifts due to material changes but also to assess their broader implications for the reliability and commercial viability of TMD-based electronics, optoelectronics, and quantum technologies. Deeper insight into such fundamental issue opens up a pathway towards developing strategies that could significantly enhance the robustness, scalability, and industrial adaptation of TMD-based devices.

## Results

### Low-field (LF) and High-field (HF) region demarcation

We intend to improve the understanding of inverse piezoelectrically induced strain leading to performance drifts in the TMD devices and to reveal its nonvolatile nature<sup>26</sup>. It was important to choose electrical stress fields to assess the effects of piezoelectricity in 2D TMD materials as operation at excessively high field would result in dominant defecting and catastrophic failure. We categorized operational regimes into low-field (LF) and high-field (HF) by analyzing the  $I_D$ - $V_D$  family of curves (Fig. 1(b)) at various  $V_G$  for the MoSe<sub>2</sub> FETs. We observed current saturation above 50 kV/cm at high gate biases and further rise in current after 120 kV/cm. These devices failed at lateral fields exceeding 140 kV/cm when high currents flowed in device (See Supplementary Note 13). We selected 40 kV/cm and 100 kV/cm as the LF and HF regimes, respectively for the electrical stress operation. We kept the gate terminal floating when devices were electrically stressed across the source-drain to minimize oxide governed effects and obtain the electrical performance drifts majorly governed by the properties of TMD itself.

The lateral stressing fields ( $E_{DS}$ ) were used in a measure-stress-measure scenario. We varied the stressing times from  $10^{-6}$  s to  $10^3$  s and extracted electrical data from  $I_D$ - $V_G$  taken pre and post stress. One set of devices was subjected to continuous measure-stress-measure cycles to discuss the nature of electrical properties drift as the electrical stress leads to evolution of device performance. A separate set of devices was subjected to single measure-stress-measure scheme with specific stress times, and these were used for analyzing drifts in material properties pre and post stressing.

### Electrical performance drifts and characteristic instabilities

The currents captured during LF and HF stress (Fig. 2a) demonstrate an incremental trend which was larger for devices under HF stress. A gradual negative shift in the charge neutrality point was observed over successive operation times (Fig. 2b, c) which seemed to settle in LF stressed devices but shifted more prominently due to HF stressing. The current transients during HF stressing showed a trend of larger shift with further operation. Our devices were decently ambipolar and performance drifts were analyzed using extracted parameters from  $I_D$ - $V_G$  taken pre and post sweeps and compared changes in electron and hole conduction.

Electron current ( $I_n$ ) increased by ~11% and ~40%, and hole current ( $I_p$ ) supported through channel decreased by ~75%, and ~95% in LF and HF stressed devices, respectively after ~1000 s of operation (Fig. 3a). Threshold voltage ( $V_T$ ) showed a progressive negative shift for n-type branches by 4.14 V and 11.16 V (Fig. 3(b)), respectively for LF and HF stresses, and a

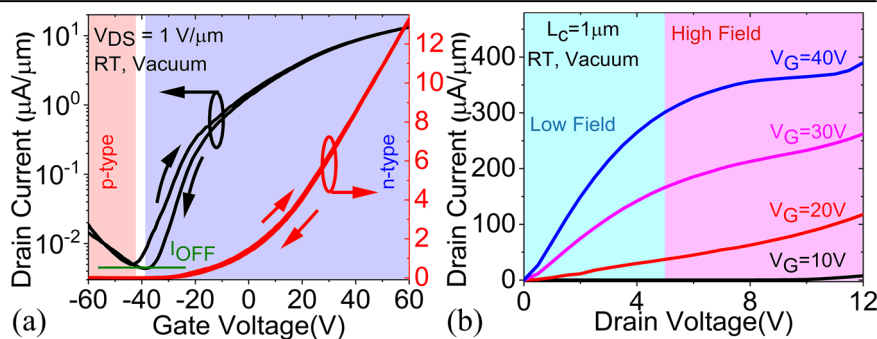
negative shift for p-type branch by 2.35 V and 5.36 V, respectively for LF and HF stresses with HF leading to sharper  $V_T$  drifts. The subthreshold slope (SS) revealed an initial degradation in electron conduction by ~17.6% which improved by ~19.7% from the peak degraded value due to LF stressing. The SS showed an initial improvement in hole conduction by ~32% which degraded by ~6.4% from peak improvement during LF stressing. The SS for electron and hole conduction improved by ~41% and ~25% due to HF stressing (Fig. 3c). The electron mobility ( $\mu_{nFET}$ ) improved by ~12%, and ~52% due to LF and HF stresses respectively, and the p-type mobility ( $\mu_{pFET}$ ) reduced by ~73%, and ~86% due to LF and HF stresses, respectively. HF stressing operation induced improvement in mobility can further increase as suggestible by the trends even after 1000 s of operation (Fig. 3d). Electrical stresses induced a consistent rise in contact resistance ( $R_C$ ) for both electron and hole conduction. LF stressing led to ~40% rise and HF operation inducing ~445% rise in  $R_C$  for electron conduction. The  $R_C$  for hole conduction consistently increased by ~250% and ~532% due to LF and HF operation respectively, which suggests an overall increase in  $R_C$  of the devices. The trend of increase in  $R_C$  establishes that longer stressing would result in larger rise in the contact resistance (Fig. 3e).

The current transients captured during electrical stress exhibited a minima of current for operation between 1 ms and 100 ms. The conduction current in 2D TMD FETs is reportedly not limited by heating at these time scales and must show larger currents instead between 1 ms and 100 ms<sup>27</sup>. Electrical operation for longer time scales (>1 s) is reported to degrade the current conduction due to self-heating, also accompanied by carrier trapping as reported in prior works<sup>6,13,27,28</sup> but we observe an increment in current instead (Fig. 2a). The stress current under HF operation did not exhibit a saturating behavior even after ~1000 s of electrical stress. The thermal conductivity of TMDs is reported to decrease at higher temperatures and tensile strains. A drop in thermal conductivity will lead to inefficient heat dissipation and more heating in the MoSe<sub>2</sub> channel during stressing leading to earlier self-heating limit on current rise<sup>29</sup>. The observed stress current rise in channel must be due to change in the MoSe<sub>2</sub> properties leading to modified thermal dissipation, carrier concentration, or strain in material as such events will dictate the current supported by the channel.

A negative shift in  $V_T$  accompanied by rising electron current and decreasing hole current suggests increased electron concentration in devices. The OFF current at charge neutrality point remains the same, suggesting the MoSe<sub>2</sub> getting affected non-uniformly in channel and contact region. The FET seems to have a localized source of 'excess' electrons as suggested by current evolution trends. The carriers for conduction in the device come disproportionately from channel and contact regions that evolve during the electrical stresses leading to drift in performance.

We used Y-function method to extract FET mobility ( $\mu_{FET}$ ) and contact resistance ( $R_C$ ) which can be included in our characterization routine of specifically timed electrical stressing cycles. The  $\mu_{FET}$  and  $R_C$  extracted using Y-function is reported to be inaccurate for 2D TMD FETs but extracted numbers can provide a fair trend for comparison<sup>30</sup>. The increment seen in electron mobility and decrease in hole mobility could be due to carrier concentration change or change in scattering due to strain which evolves

**Fig. 1 | Electrical characteristics of our ambipolar MoSe<sub>2</sub> FETs and field intensity estimation used in this study.** **a** Typical transfer characteristics of MoSe<sub>2</sub> FETs used in the study. Our devices were ambipolar with distinctive n-type and p-type conduction regimes and OFF current measured at the charge neutrality point. **b**  $I_D$ - $V_D$  family of curves highlighting LF regime below 50 kV/cm and HF regime above 50 kV/cm. Operational fields above 140 kV/cm across drain and source led to catastrophic failure.



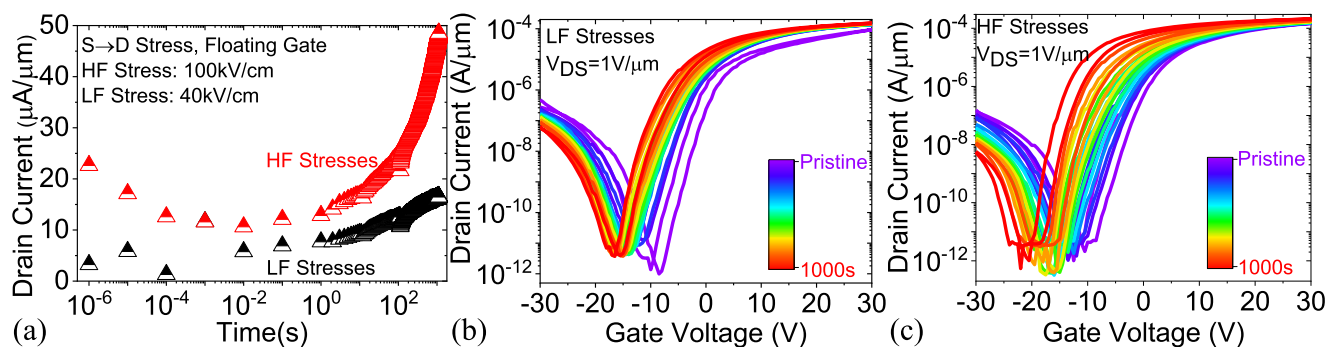


**Fig. 2 | Signatures of non-volatile drifts in electronic performance under low and high field and its temporal evolution.** **a** Current–time trends captured during stressing the MoSe<sub>2</sub> FETs across operational time scales exhibited a higher current rise (approx. 3×) during HF stressing as compared to LF stresses. Transfer

characteristics of ambipolar devices in between stresses show evolution of electronic characteristics due to electrical stresses **b** Low field operation and **c** High field operation. HF stresses lead to more drastic shifts as compared to LF stresses.

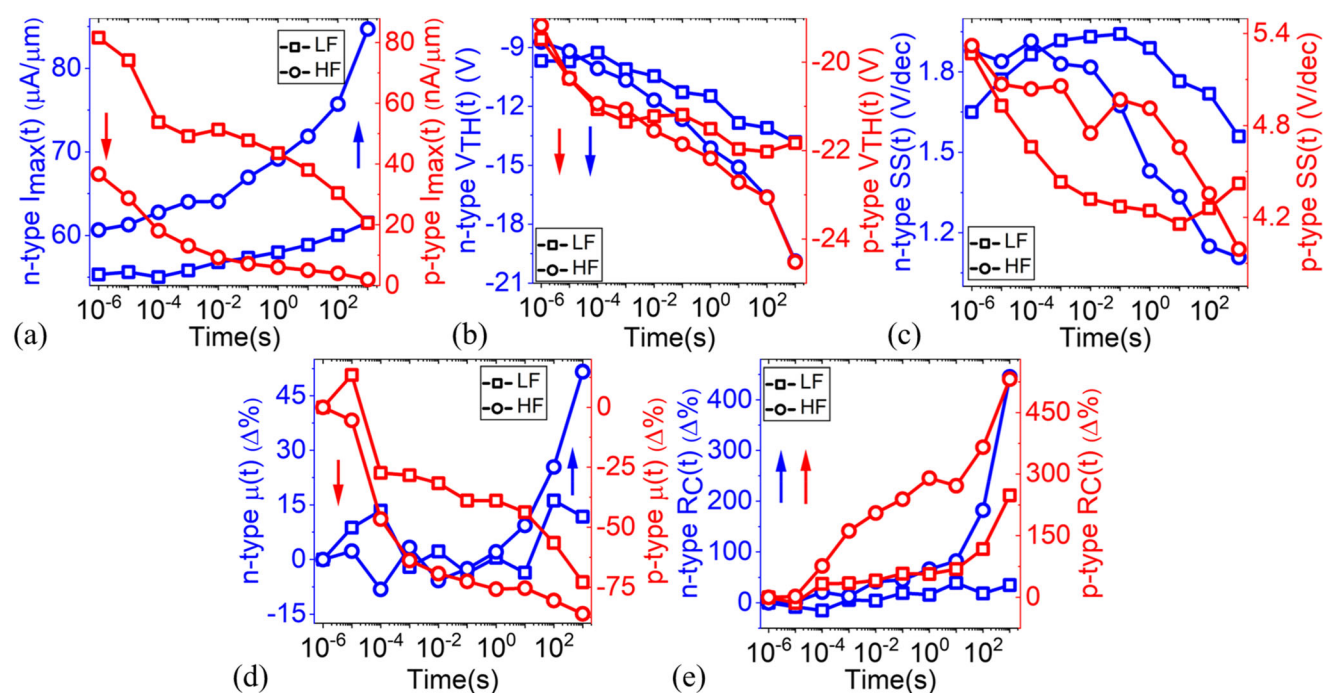


**Fig. 3 | Evolution of electrical parameters due to LF and HF stressing during 10<sup>−6</sup>s to 10<sup>3</sup>s.** **a** The electron current increased (~40%) and hole current decreased (~95%) in devices due to stressing, **b** Threshold voltage ( $V_T$ ) shifted negatively for both electron and hole current branches (~11V, ~5V respectively), **c** Subthreshold swing (SS) degrades initially and then improves for electron conduction due to LF stressing. SS improves initially and then degrades for hole conduction due to LF stressing.

HF stressing improved SS for both electron and hole conduction by ~36% and ~24%, respectively **d** Electron mobility improved by ~53% and hole mobility degraded by ~86% due to stressing, and **e** Contact resistance increased for electron conduction and hole conduction by ~445%, and ~532%, respectively. The performance drifts increase over time of operation with higher drifts seen at higher fields.

with time<sup>31,32</sup>. The change in currents and mobilities while increasing  $R_C$  points to the contact region being a factor leading to performance drifts as  $R_C$  for electron conduction should decrease if the material gets a uniform increase in electron concentration.

The material characterization and analysis presented further reveals a work function change due to differing strain in channel and contact regions of device. This distinct strain led to changes in band-structure in the channel and contact regions that manifested as increased  $R_C$  coupled with improvements in electron conduction and degradation in hole conduction<sup>33</sup>. The direction of the electric field under contact is vertical whereas the electric field direction in channel remains horizontal in our planar FET. This leads to differing strain in the material under contacts and channel which explains the rise in  $R_C$ <sup>33</sup> as the inverse piezoelectric coefficients have a dependency on the electric field vector<sup>25</sup>.

Increased  $R_C$  leads to a higher potential drop at the contact-channel interface leading to further increase in strain at the interface during electrical operation, resulting in further performance drifts seen in HF stressing case.

#### Inverse piezoelectricity induced strain in MoSe<sub>2</sub> channel

We used key parameters from Raman spectroscopy like peak position, shift, and full width half maximum (FWHM) to assess change in strain, carrier concentration, and defects in the MoSe<sub>2</sub> crystal in the channel<sup>34,35</sup>. We assessed the MoSe<sub>2</sub> channel using the out of plane vibration Raman active mode ( $A_{1g}$ ) which were taken before and after the measure-stress-measure cycle for every device. The changes in peak position of  $A_{1g}$  Raman active mode exhibits combined signatures of carrier concentration, strain, defecting in TMDs. Linewidth (FWHM) is used to assess crystallinity of the



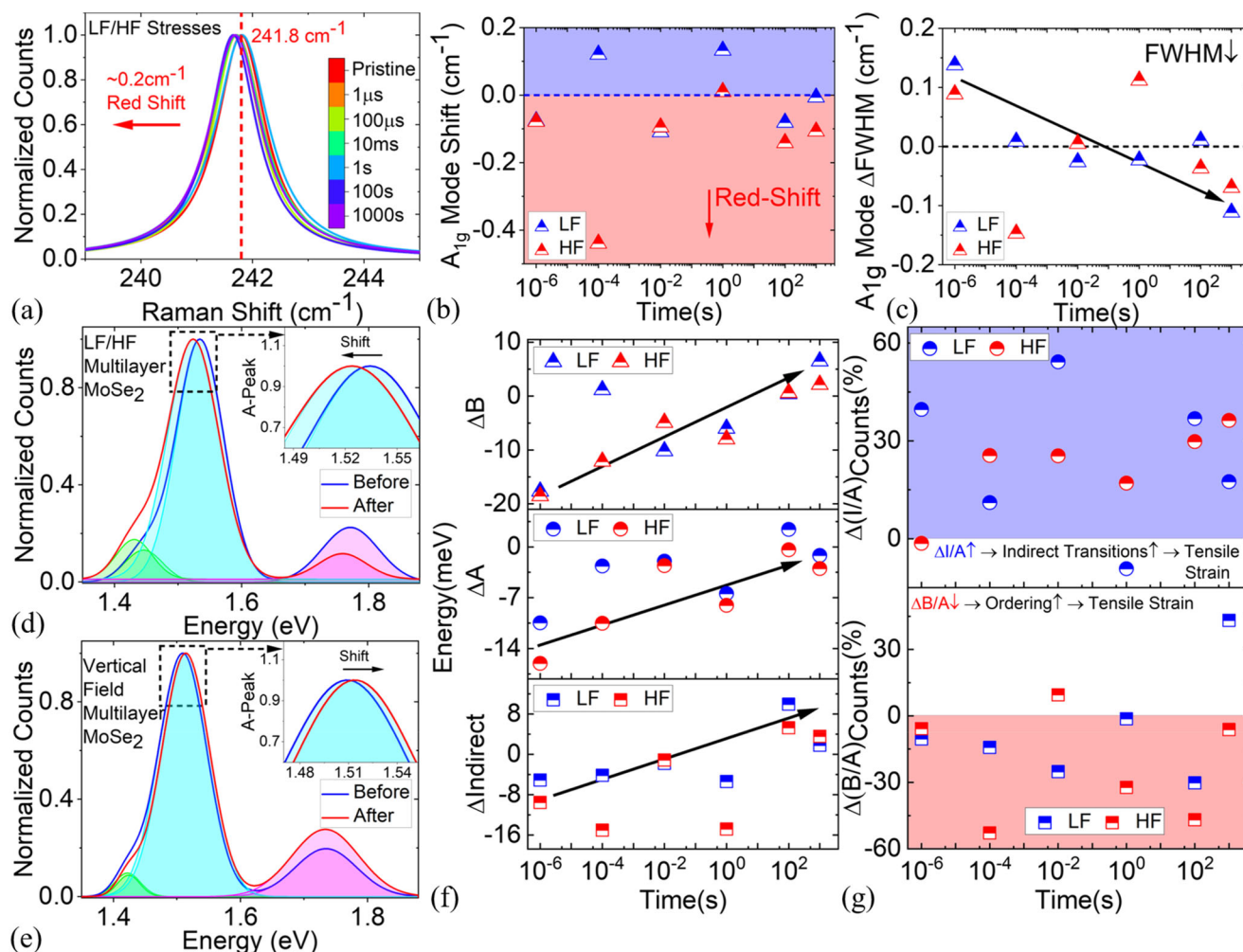


**Fig. 4 | Shifts in  $A_{1g}$  Raman peak and PL spectrum captured after stressing devices for distinct operational times.** **a**, **b**  $A_{1g}$  peak of  $\text{MoSe}_2$  in channel was red shifted ( $\sim 0.2 \text{ cm}^{-1}$ ) due to the electrical stressing, **c** FWHM decreased by  $\sim 0.2 \text{ cm}^{-1}$  which indicates the channel does not degrade, rather the crystallographic ordering improves due to stressing, **d** PL spectra reveal a shrinkage in bandgap ( $\sim 18 \text{ meV}$ ) and increased indirect bandgap contribution due to electrical stressing, **e** PL spectra

from “under the contact” scanned region (using high voltage AFM) revealed an increase in bandgap ( $\sim 5 \text{ meV}$ ) due to vertical electrical field. **f** Electrical stressing led to shrinkage in the energy of optical transitions (A, B, and indirect transitions). **g** The I/A and B/A counts ratio increased and decreased, respectively, which suggested tensile strain and increased ordering in channel because of electrical stresses.

material and change in defect signature which would be governed by degradation or strain.

We captured the evolution of  $A_{1g}$  peak from  $10^{-6}$  s to  $10^3$  s operation, where the  $A_{1g}$  mode exhibited a red shift of  $\sim 0.1 \text{ cm}^{-1}$  due to the electrical stressing (Fig. 4a, b). We noticed a gradual decrease in FWHM of  $A_{1g}$  mode due to the stresses (Fig. 4c). The red shifts in the  $\text{MoSe}_2$  in channel appeared instantaneously as seen after  $1 \mu\text{s}$  stressing. The shorter time scales of operation led to an increase in FWHM of  $A_{1g}$  mode which later reduced as the stress time increased. There was a red shift in  $A_{1g}$  peak of TMDs with increased FWHM suggesting increase in defects, increased electron carrier concentration, or release of strain in the  $\text{MoSe}_2$ . Like  $\text{MoSe}_2$ ,  $A_{1g}$  mode in  $\text{MoS}_2$  exhibits red shift in case of increased electron carrier concentration<sup>35</sup>. Further electrical stressing led to red shift in the  $A_{1g}$  mode along with decrease in FWHM corresponding to uniaxial tensile strain in  $\text{MoS}_2$  either in armchair or zigzag direction<sup>34</sup>.  $\text{MoS}_2$  has  $E_{1g}$  Raman active mode as well which can assist in identifying if the armchair or zigzag direction develops tensile strain. However,  $\text{MoSe}_2$  has only  $A_{1g}$  Raman active mode and we analyzed the features of  $A_{1g}$  mode only.

The electrical stress resulted in consistent red shifts accompanied by reduction in FWHM suggesting that the channel did not show an increase in defects or faced degradation in thermal properties. The  $\text{MoSe}_2$  in channel got tensile strained that resulted in an increased carrier concentration. The

possibility of increased number of defects in  $\text{MoSe}_2$  in channel is ruled out based on decrease in FWHM of the  $A_{1g}$  mode<sup>36</sup>. The in-plane tensile strain in  $\text{MoSe}_2$  is reported to result in reduction of thermal conductivity of material<sup>29</sup>. This degradation in thermal properties should result in red shift of  $A_{1g}$  mode with increased FWHM of  $A_{1g}$  mode of  $\text{MoSe}_2$  due to laser heating and poorer heat dissipation during Raman spectrum capture<sup>37</sup>. We ruled out the dominance of degradation of thermal properties based on overall red shifts and decrease in FWHM of  $A_{1g}$  mode for  $\text{MoSe}_2$  channel which established a dominance of in-plane tensile strain signature. The behavior of  $A_{1g}$  Raman peak still encompassed a combined signature of carrier concentration and strain information<sup>35,38</sup>. The in-plane tensile strain led to a rise in carrier concentration which is responsible for rise in electron current during stressing, however the suspected decrease in thermal conductivity must limit the current rise during stressing. We observed an increase in stress current for both LF and HF stressed devices for  $10^3$  s suggesting that the degradation in thermal properties of channel is not dominant, if any. The  $\text{MoSe}_2$  under the contact must be getting strained in a different manner than channel resulting in possibly increased thermal conductivity as compared to  $\text{MoSe}_2$  in channel dominating the electrical drifts observed during stress.

Further, any change in bandstructure of channel material due to straining at K-point can be verified using PL spectrum from  $\text{MoSe}_2$  in

channel. A detailed Raman map denoting red shift of  $A_{1g}$  peak shows the distribution of strain (and resultant change in carriers) suspected in the device. However, getting spatial resolution using such micro-Raman technique is challenging as the shifts in  $A_{1g}$  mode are minimal but can be seen using skew in  $A_{1g}$  peak map (See Supplementary Note 2).

### Bandstructure evolution under strain

Photoluminescence (PL) is a dominant phenomenon in 2D TMDs in response to optical excitation where multilayer TMDs exhibit both direct and indirect transition components. Few layered  $\text{MoSe}_2$  used in our devices showed A-exciton ( $\sim 1.51$  eV) which is direct band transition at K-point, B-exciton ( $\sim 1.75$  eV) which is another direct band transition at K-point due to higher energy degenerate bands, and indirect bandgap ( $\sim 1.41$  eV) transition, which is either from K-to- $\Gamma$  or from A-to-K as the number of layers increase and as the strain changes in  $\text{MoSe}_2$ <sup>39–42</sup>. The B/A-exciton count ratio is indicative of the amount of crystallographic disorder or defects in the material<sup>43</sup>.

Deconvoluted PL from the channel indicated a shrinkage of bandgap due to electrical stress (Fig. 4d). The A-exciton peak indicated a decrease in direct bandgap by  $\sim 18$  meV after devices are electrically stressed (Fig. 4d, f). The indirect bandgap shrunk by  $\sim 15$  meV and there was an increased proportion of indirect band transitions after electrical stress on  $\text{MoSe}_2$  channel. The B/A-exciton count ratio decreased to 0.1062 from the pristine value of 0.2251 after electrical stress. The ratio of indirect-to-direct bandgap transition count increased to 0.1651 from 0.1315 after electrical stress (Fig. 4g). For the assessment of  $\text{MoSe}_2$  under the contact that experiences vertical electric field during stressing, a multilayer  $\text{MoSe}_2$  flake was scanned with high voltage applied on AFM tip in contact mode during scanning to mimic vertical field under contact. The A-exciton peak exhibited an increase in direct bandgap by  $\sim 4.7$  meV (Fig. 4e). The indirect bandgap increased by  $\sim 1.7$  meV, and the indirect-to-direct bandgap transitions decreased to 0.0876 from 0.0966 after the vertical field applied. The B/A-exciton ratio increased to 0.27608 from 0.01388 after the high voltage vertical field applied was applied on the flake.

The PL spectrum obtained at various times across the electrical operation exhibited a decrease in bandgap and decrease in B/A-exciton count ratio from the  $\text{MoSe}_2$  in channel. The initial operation introduced a greater amount of bandgap shrinkage while decreased B/A ratio does not change much with operation<sup>41,44</sup>. Further operation led to a decrease in amount of shrinkage in bandgap, decrease in the B/A-exciton ratio, and increased indirect transitions suggesting the accumulation of in-plane tensile strain in the TMD channel material, which is applicable to all popular TMDs<sup>40,41,44</sup>. Electrical stresses induced tensile strain in channel facilitating a tightening of  $\text{MoSe}_2$  crystal in the channel, also implied by the decrease in FWHM of  $A_{1g}$  Raman mode (Fig. 4c, g). Decrease in B/A-exciton count ratio indicates a reduction in number of defects, we argue that the tensile strain led tightening of TMD crystal in channel leads to reduction in signature of defects as no extrinsic passivation has been performed. The  $\text{MoSe}_2$  layers in the channel exhibit increased ordering in the crystal due to the tensile strain rather than a change in number of defects in the channel. The HF operated device had a greater reduction in B/A-exciton count ratio than LF operated device due to higher tensile strain as seen by greater lowering in the ratio.

The electrical trends suggested an increase in electron concentration, and PL spectrum can be used to comment on the carrier concentration in the material. The trion to exciton peak energy separation is a good indicator of carrier concentration in the TMDs<sup>45</sup>. But we had a PL spectrum from multilayer  $\text{MoSe}_2$  channel where the indirect transition peak of  $\text{MoSe}_2$  lies very close to A-exciton peak and it is difficult to reliably fit a trion peak and distinguish the transitions from indirect transitions<sup>46</sup>. Thus, we cannot directly comment on the electron concentration using trion to exciton ratio for a multi-layer  $\text{MoSe}_2$  channel. However, indirect bandgap transitions are strain sensitive in TMDs which increases with bandgap reconfiguration due to tensile strain<sup>39</sup>. Various studies reported the bandgap shrinkage with respect to tensile strain in monolayer  $\text{MoSe}_2$  to be 42 meV/%<sup>40</sup>, and 27 meV/%<sup>47</sup>, and our analysis estimate the in-plane tensile strain to be  $\sim 0.3$

0.5% in the  $\text{MoSe}_2$  channel in accordance with previous reports. We performed PL spectral mapping of LF, HF stressed, and unstressed devices which clearly show an improved and degraded crystallinity in  $\text{MoSe}_2$  near channel and contacts, respectively, according to the B/A-count ratio metric (Supplementary Fig. 3).

In contrast to the lateral electric field in  $\text{MoSe}_2$  channel where a decrease in bandgap was found, we estimated an increase in bandgap due to vertical field applied to  $\text{MoSe}_2$  using high potential contact mode AFM over multilayer  $\text{MoSe}_2$  flake. This vertical field scenario mimics the field experienced by the TMD under the contact (Fig. 4e and Supplementary Figs. 13, 14, 15, and 16). We observed a decrease in the indirect to direct exciton transitions, with an increase in B/A ratio for the  $\text{MoSe}_2$  under contact due to the vertical field. The  $\text{MoSe}_2$  under the contacts gets compressively strained up to  $\sim 0.1$ – $0.2\%$  due to applied potential of up to 30 V for a 3  $\mu\text{m}$  channel to realize the HF operational field condition<sup>40,47,48</sup>.

The exfoliated  $\text{MoSe}_2$  on  $\text{SiO}_2$  usually has an initial tensile strain of  $\sim 0.4\%$  which is reported for various substrates in prior studies<sup>49,50</sup>. The  $\text{MoSe}_2$  in channel accumulates  $\sim 0.5\%$  of additional in-plane tensile strain which must reduce the thermal conductivity<sup>51,52</sup>. This reduced thermal conductivity would lead to higher heating of the channel and limit the rise in stress current. However, the  $\text{MoSe}_2$  under the contact accumulates up to 0.2% compressive strain over the initial strain due to substrate. This leads to an increase the thermal conductivity<sup>51,53</sup>. The increase in the thermal conductivity of  $\text{MoSe}_2$  under contact dominates as it dissipates heat to metal contact and substrate whereas  $\text{MoSe}_2$  in channel with reduced thermal conductivity dissipates only to substrate below and vacuum from top. We conclude that either the  $\text{MoSe}_2$  properties at contact dominate the observed parameter drifts or the drift in thermal properties channel does not dominate over the competing strain mechanism. Prolonged operation once the strain manifests in channel and contacts completely during electrical operation results in higher heat generation in channel due to reduction in thermal conductivity of channel. The increased local temperature could lead to thermal generation of defects which increases the piezoelectric response of the material<sup>54</sup>. Apart from defects, the local heating would increase local piezoelectric response leading to higher strain<sup>25</sup>. The presence of this positive feedback mechanism would promote a defect mediated failure as previously reported for TMD devices at high fields<sup>12,55</sup>.

### Implications on $\text{MoSe}_2$ channel surface potential and workfunction

Kelvin Probe Force Microscopy (KPFM) maps with high spatial resolution were obtained before and after stressing the respective devices which revealed drift in the work function of  $\text{MoSe}_2$  in the channel due to the electrical operation. Similarly, we mimicked the ‘under the contact’ scenario to assess the effect of vertical field on  $\text{MoSe}_2$  to build a complete picture of phenomena being observed (Supplementary Note 9).

The  $\text{MoSe}_2$  in channel showed a higher WF ( $\sim 35$  meV) than the Pd contact electrodes (Fig. 5a, d) in a pristine device. 1000 s of LF operation across the device introduced a uniform decrease in WF in channel by  $\sim 400$  meV which had a sharp dip near contact edges (Fig. 5b, d). 1000 s of HF operation led to seemingly lesser reduction in WF in center of channel but had a very sharp profile of decreased WF near the drain edge. There was a reduction of  $\sim 50$  meV at the center of channel whereas the WF of  $\text{MoSe}_2$  near drain edge reduced by  $\sim 350$  meV (Fig. 5c, d). The  $\text{MoSe}_2$  channel experienced a decrease in WF due to electrical operations, and the WF further decreased sharply near the drain edge due to HF operation resulting in high WF mismatch in the device. A higher operating field induced greater strain governed WF decrease near drain edge which extended into the channel ( $\sim 700$  nm) to affect a larger area in the  $\text{MoSe}_2$  channel. Decreased WF of channel with prominent dip in WF near the contact edges signify emergence of tensile strain in  $\text{MoSe}_2$  leading to increased electron concentration in tensile strained area in  $\text{MoSe}_2$  channel<sup>56</sup>. The  $\text{MoSe}_2$  under the

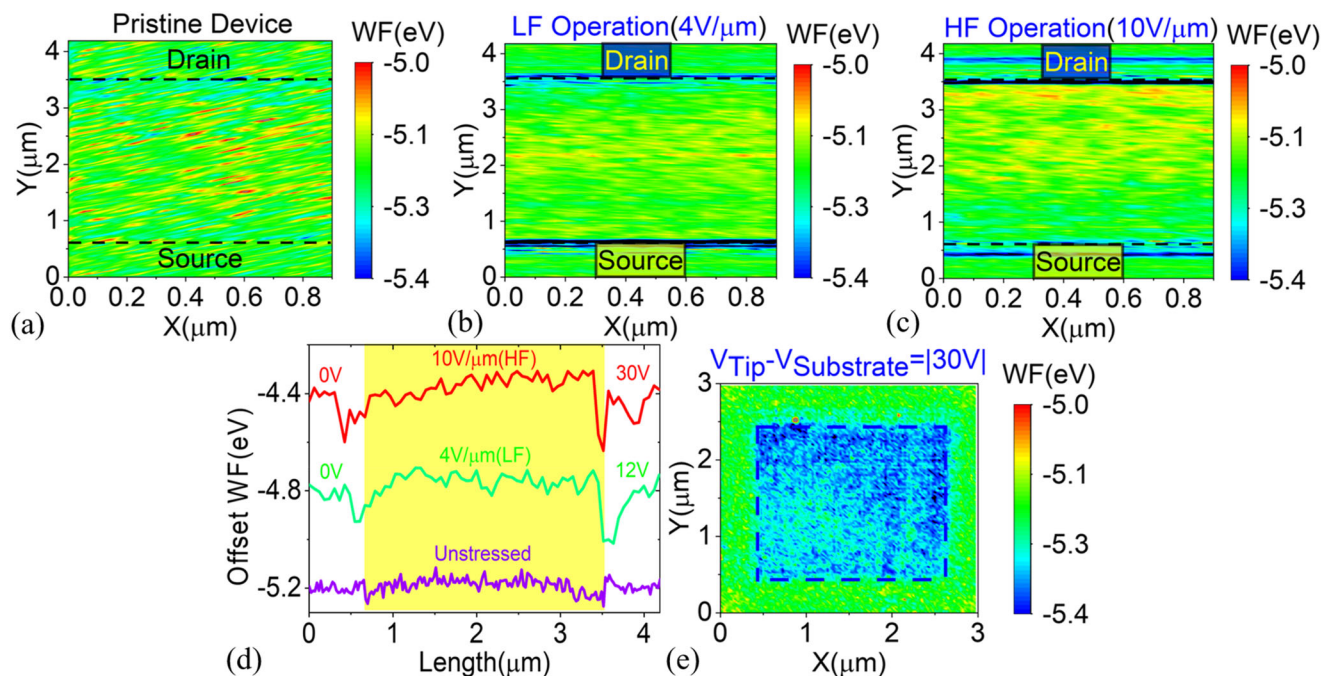


**Fig. 5 | Distinction in evolution of work function of MoSe<sub>2</sub> in channel due to lateral low and high field and under/near contact due to vertical field.** Work function (WF) scans of the devices on exfoliated multilayer MoSe<sub>2</sub> using KPFM reveals WF change in the channel due to LF and HF stresses, **a** WF map of an unstressed device, **b** WF map of LF stressed device, **c** WF map of HF stressed device,

**d** Averaged line data from (a–c) shows sharp mismatch of WF arising due to LF/HF operation with higher dip near the drain edge, **e** Increased WF is seen in the 2 × 2 μm<sup>2</sup> region after scanning the area with high potential applied between tip and MoSe<sub>2</sub> flake (vertical field) using contact mode AFM scan on the multilayer MoSe<sub>2</sub>.

contact that experienced vertical field exhibited an increase in WF by ~117 meV, for a multilayer MoSe<sub>2</sub> flake. The HF stressed device showed a WF scan which has contribution from lateral field induced tensile strain and very high vertical field induced compressive strain extending into the channel away from electrode leading to lesser WF lowering than LF stressed device but a sharper WF mismatch profile.

We estimated a decrease in WF of MoSe<sub>2</sub> in channel due to tensile strain, yet we observed an increase in the contact resistance extracted from the electrical trends. A uniform decrease in WF of TMD across the device must result in decreasing trend in  $R_C$ , we observe an increase in  $R_C$  instead. The MoSe<sub>2</sub> under the contact was investigated using high voltage contact mode AFM scanning to mimic 30 V applied vertically on drain in a 3 μm device (HF operation condition of  $V_{DS} = 10$  V/μm). This vertical electric field introduced compressive strain in the MoSe<sub>2</sub> under the contact leading to an increase in the work function. Similar observation was reported earlier for MoS<sub>2</sub> where defecting introduced strain to change work function<sup>57</sup>. Electrical stress does not introduce defects in our case. This region under the contacts becomes p-type in nature due to the increase in work function (Fig. (5e), Supplementary Figs. 13 and 15). Whereas electrically, the channel becoming n-type dominates the observed drifts in electrical operation<sup>56</sup> (Supplementary Figs. 12, 13, 14, 15 and 16).

### Recovery and nonvolatile nature of strain

We reported a distinct reduction in hole current that was observable to a drastic extent in HF stressed devices. The tensile strain in MoSe<sub>2</sub> channel led to an increase in n-type nature of channel whereas the MoSe<sub>2</sub> under contacts developed a p-type nature due to compressive strain. The hole conduction branch suffered due to the decreased work function of MoSe<sub>2</sub> channel in the devices during electrical stress. The parameter drifts remained in the devices when assessed post stress establishing that the tensile and compressive strain in channel and under contacts to be non-volatile, respectively. We needed to observe and check if any recovery in channel and electrical characteristics is observable due to crystal relaxation post stressing. From prior knowledge,

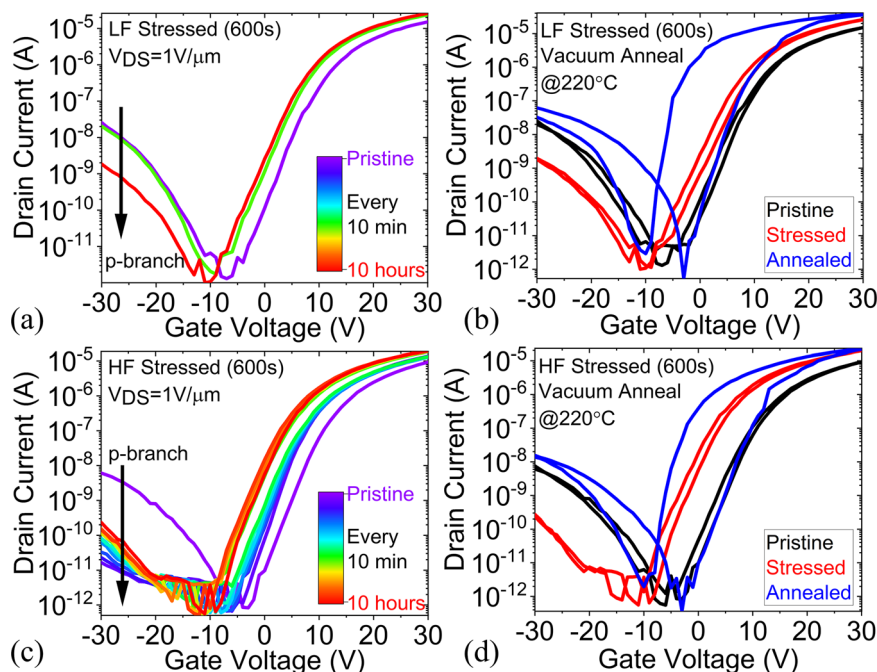
the trap capture and emission time constants for the oxide traps are usually in the order of 10<sup>3</sup> s. The traps due to interface, defects and adsorbates interact faster and contribute to transient performance drifts and get detrapped in similar time scales. However, most of the traps are reported to introduce volatile performance drifts and exhibit recovery in the electrical performance<sup>6,58</sup>. We allowed the stressed devices to recover in an unperturbed state after removal of electrical stress in RT, vacuum and subsequently used vacuum annealing treatment to provide heat energy for the crystal recovery.

We followed the similar measure-stress-measure routine to electrically stress the devices for 10 min (600 s) under LF and HF operation and then monitored the electrical parameter drift by measuring  $I_D V_G$  every 10 min for a period of 10 h without applying further electrical stress. It took ~3 h for the electrical drifts to settle in LF stressed device (Fig. 6a). HF stressed device showed a larger drift in performance taking ~5 h for the drifts to settle (Fig. 6c). HF operation deteriorated the hole conduction immediately and the LF operation degraded the hole current slightly. The devices did not exhibit any self-recovery in RT vacuum condition even if left undisturbed for ~10 h after LF/HF operation retaining the strain with no recovery observed in hole conduction.

The stressed devices were then vacuum annealed at 220 °C with slow upramp and downramp of temperature for 10 h (with 6 h at ~220 °C) as thermal energy can provide relaxation energy for the strained crystal and help in recovery. We chose these annealing parameters to be compliant with standard fabrication processes that do not degrade the MoSe<sub>2</sub> in devices<sup>59</sup>. We assessed the performance of these annealed devices. An immediate observation was the overshoot in hole conduction branch post annealing, i.e., higher hole currents were observed after annealing the stressed devices, with steeper subthreshold slopes. A large hysteresis in transfer curve as high as ~10 V was observed which was ~1 V before annealing (Fig. 6b, d). The recovery trends suggests that the compressive strain in the MoSe<sub>2</sub> under contact did not relax as a huge improvement in p-type current is observed whereas the tensile strain in the channel relaxed to some extent due to which the channel supported a higher hole current than before. The MoSe<sub>2</sub> under



**Fig. 6 | The electrical performance exhibits drift for several hours (sampled every 10 min) after electrical stressing of 600s.** **a** LF stressing induces electrical drifts which take ~3 h to settle. **b** Attempt of electrical performance recovery of LF stressed devices using vacuum annealing introduces a large hysteresis in performance accompanied by an overshoot in hole conduction. **c** HF stressing induces large electrical drifts in ~5 h starting with instant suppression of hole conduction branch. **d** Recovery attempt of HF stressed using vacuum annealing introduces large hysteresis with an overshoot in hole conduction.



contact is constrained by metal on top and bottom substrate preventing a complete release of compressive strain. The MoSe<sub>2</sub> channel is constrained by substrate interaction at bottom interface only and is suspected to relax more than the contact region. The annealing led recovery is understandable based on differences of strain induced in contact and channel area with a difference in freedom for MoSe<sub>2</sub> crystal to relax.

With respect to carrier trapping, when the carriers are trapped/de-trapped in the device during electrical stress, a recovery trend is noticeable when the traps return to their respective relaxed state post stressing. This nature of trap relaxation would have manifested as a noticeable positive shift of  $I_D V_G$  characteristics after negative shift introduced in our devices by electrical stress as reported in previous works<sup>6,60</sup>. We observed non-volatile negative shifts in  $I_D V_G$  with time elapsed post stress suggesting the manifestation of strain to dominate over the previously reported causes of performance drifts in 2D TMD devices at discussed electric fields. The traps are not expected to introduce further performance drifts once the electrical stress is removed, and the device is kept in an unperturbed state.

Recovery studies reveal a requirement of finite time for strain to manifest itself and affect the electrical properties after the MoSe<sub>2</sub> FETs are electrically stressed. The emergence of widened hysteresis post thermal annealing can be attributed to the enhanced n-type and p-type nature of channel and contact, respectively, leading to WF mismatch of MoSe<sub>2</sub> in device. There is an uneven recovery of MoSe<sub>2</sub> lying in channel and under contacts leading to uneven carrier concentrations. The electric field vector under contact and channel invokes the out-of-plane and in-plane coefficients from the piezoelectric tensor of MoSe<sub>2</sub>, respectively. This gives rise to varying inverse piezoelectric response in different regions leading to compressive strain under contacts and tensile strain in the channel due to direction of field lines in the device. We studied the non-volatile straining due to electrical operation and its implication under various conditions and presented them in supplementary notes (Supplementary Notes 4, 5, and 11).

## Discussion

The electrical performance instabilities are rooted to strain arising from interaction between electric fields and piezoelectric properties of TMDs establishing a fundamentally inevitable source of instability in TMD based devices. Our observations establish that the MoSe<sub>2</sub> in the device immediately responds to the applied electrical stress. The lateral field introduced tensile strain in the channel and the vertical field introduced compressive strain under contact due to inverse piezoelectricity of MoSe<sub>2</sub> and required

finite time to come into effect. The tensile strain in channel is confirmed by decreased FWHM, and red shifts in A<sub>1g</sub> Raman mode. Photoluminescence spectrum confirms decrease in bandgap, improved crystallographic ordering and reduced signature of defects in form of decreased B/A-exciton count ratio in channel. Increased indirect transitions in PL spectrum provide strong evidence of tensile strain. As a result of the tensile strain, we observed a decrease in the work function of the MoSe<sub>2</sub> channel post electrical stressing.

Contrary to the inverse piezoelectricity induced tensile strain in channel, the MoSe<sub>2</sub> experiences compressive strain due to the vertical electric field under the contact. The compressive strain is confirmed using PL spectrum where the bandgap increases, crystallographic disorder increases which shows up as increased B/A-exciton count ratio. An increase in work function because of compressive strain is observed in MoSe<sub>2</sub> due to vertical electric field at contact due to electrical stress. The FET performance drifts arise due to an increase in TMD work function under the contact due to compressive strain and decrease in TMD work function in channel due to the tensile strain. This work function mismatch was found to evolve with time during electrical stressing. HF electrical operation led to greater decrease in work function near the drain edge as compared to LF stress. This contributed to instantaneous decrease in hole conduction observed in electrical results. The trends of electrical drifts suggest a 'runaway' drift according to stress current transients. The contact resistance ( $R_C$ ) increases over stressing period which intensifies heating and higher potential drops at channel-contact interface. Both heating and higher potential drop at channel-contact interface would lead to higher localized strain near contact edges. During the electrical stressing, heating and different nature of strain under contact and in channel can lead to rupture of TMD near contacts. The inverse piezoelectric strain introduces a non-volatile shift in electrical performance which cannot be recovered due to constrictions on the TMD in the device architecture.

The reason for the differing nature of strain in the TMD under contact and in channel can be understood by referring to the inverse piezoelectric tensor for such TMDs. A reference inverse piezoelectric tensor for monolayer TMD crystal comprises of non-zero coefficients in form of  $d_{11}$ ,  $d_{12}$  and  $d_{26}$ , where  $d_{11} = -d_{12} = -d_{26}/2$ . The subscripts '1', '2', '3', '4', '5', and '6' refer to 'x', 'y', 'z', '-x', '-y', and '-z' crystallographic directions. Where 'x', 'y', and 'z' correspond to armchair, zigzag, and out-of-plane directions of TMD crystal. The subscript 'xy' in a coefficient  $d_{xy}$  signifies the direction of applied electric field in 'x' direction and the resultant displacement in the 'y'

direction and the unit of  $d_{xy}$  is pm/V. Most of the previous reports disregarded the out-of-plane coupled piezoelectric coefficients, however, there have been predictions that large out-of-plane inverse piezoelectric coupling in form of  $d_{31}$  and  $d_{33}$  exists in MoSe<sub>2</sub> with realistic defects. The  $d_{33}$  coefficient is predicted to have exceptionally large values when realistic defects and disorders are considered<sup>25,26</sup>.

Our multilayered MoSe<sub>2</sub> is expected to be strained due to interaction of  $d_{11}$ ,  $d_{12}$ ,  $d_{26}$ <sup>34</sup>,  $d_{31}$ , and  $d_{33}$ <sup>25</sup> in response to different electric field directions encountered under contacts and in channel. The straining under contacts is governed by a large  $d_{33}$ , and negligible  $d_{31}$  coefficient, and the straining in channel is governed by  $d_{11}$ ,  $d_{12}$ , and  $d_{26}$  coefficients. The multilayered MoSe<sub>2</sub> under contact gets tensile strained in out-of-plane direction due to the out-of-plane electric field existing under contacts, which results in an in-plane compressive strain governed by  $d_{33}$  coefficient. Whereas the multilayered MoSe<sub>2</sub> in channel gets tensile strained in armchair direction due to  $d_{11}$ , compressively strained in zigzag direction due to  $d_{12}$  ( $=-d_{11}$ ), and compressively strained in (-) out-of-plane direction due to  $d_{26}$  ( $=-2d_{11}$ ) coefficients. Overall, with respect to in-plane direction of TMDs, compressive strains appear in material under contact and tensile strains appear in the channel which alters the electrical properties of TMD FETs.

Some prior reports use this piezoelectric property of TMDs to tune the performance of FETs by introducing mechanical strain to the channel where the strain induced in channel is kept low<sup>56</sup>. Some previous works on TMD channel breakdown at high field operation discussed the possible role of piezoelectricity in gradual degradation leading to failure but the possible dynamics were not explored<sup>12,55</sup>. The role of capping layers over channel to controllably strain TMD channel to tune its electrical properties has garnered attention from research community<sup>61–63</sup>, further unveiling unintended strain at the metal contacts formed with channel<sup>64,65</sup>. The dynamic and variable strain introduced during electrical operation of the TMD FETs reported in this study has become a considerable factor in quest of reliable TMD-based electronic technology.

The piezoelectric coefficients increase by a large margin when realistic defects in materials are considered which are present in a CVD grown TMD<sup>25</sup>. The upcoming semiconductor devices will be designed to consist of a few tens of nm channel lengths and operating  $V_{DD} \sim 0.6$  V according to IRDS, leading to an electric field of 300 kV/cm (assuming  $L_C = 20$  nm)<sup>66,67</sup>. This is a large electric field across the TMD channel at the relevant technology node can introduce variable local strain in the TMD material. Most upcoming technologies like FinFETs, complementary FETs (CFETs) and other gate all-around (GAA) architectures require edge contact to the TMD channel at source/drain instead of a top contact over TMD channel. This will reduce the region of TMD that would experience a vertical field limiting the compressive strain near contacts. While the advancements in the TMD-contact interface continue, a Schottky barrier at contact would lead to a huge potential drop at contacts. A high field near contact would introduce a high local tensile strain near contacts in the TMD leading to failure at lower electric field. If a low Schottky barrier or ohmic contact is achieved, the large electric field will exist through the channel instead of at contacts leading to a distributed tensile strain in channel<sup>65</sup>. The spacing between gate and source/drain dictates the intensity of out-of-plane electric field through the TMD material between gate and source/drain contacts where a compressive strain would exist. The usage of high- $k$  dielectrics can lower the amount of electric field in the TMD channel and reduce the electrical instabilities due strain in the TMD channel as compared to low- $k$  dielectrics, especially in the OFF state<sup>68,69</sup>. Understanding of the strain generated in TMD channel due to electric field vectors present in an architecture would become necessary to improve the technology robustness.

Different target applications using 2D TMD devices demand a variety of operating conditions that can vary the expected electrical instabilities introduced due to strain introduced during electrical operation. While the discussion in the presented work revolves around a planar FET, the findings on inverse piezoelectric strain apply to other applications using TMDs as channel. The high-speed optoelectronic devices operate in channel depleted state (OFF state) and high field across the TMD channel that would result in

high electrical instability due to straining in TMD<sup>70</sup>. The magnitude of local strains in the TMD channel depending on local field directions would be very high that can instigate defect mediated failures<sup>12,55</sup>. The devices based on heterostructures of TMDs have either vertical or horizontal heterojunction, the local electric field across the junction can introduce either compressive strain (vertical junction) or tensile strain (horizontal junction) led instabilities<sup>70</sup>. The TMDs provide a novel and efficient way of 3D integration of devices which can include multiple interfaces over the TMD channel<sup>71,72</sup>. The growth or stamping of layers over TMDs results in stress in channel and provide a constrained environment to the material. Such 3D integrated 2D TMD-based devices will again exhibit an operationally induced strain that would be distinct from behavior shown by a discrete device. Newer governing variables like initial stress, constraining environment, and dielectric properties of capping layers, among some factors, can change the degree of interaction between electric fields and piezoelectric coefficients<sup>54,65</sup>. The heterogeneous integration of 2D TMD devices with multiple functionalities requires a robust electric field isolation solution which can protect a device from instabilities induced by operation of adjacent devices operating at different conditions. The structural properties, i.e., elasticity and piezoelectricity, vary with operating temperature<sup>54</sup>. The expected strain in TMDs decreases at lower temperatures and the straining can increase at higher temperatures according to our measurements discussed in supplementary note 5. 2D TMDs used for flexible electronics applications would require due consideration of the effects due to strain and its dynamic nature during operation. The estimation of reliable operating conditions for a target application using 2D TMD technology must account for possible strain-induced instabilities in performance.

Our study provides a qualitative nature of the inverse piezoelectricity-induced device stability concern that arises during electrical operation. The quantitative extent of instability induced in electrical performance can vary due to material quality, quality of interfaces, device architecture, and target application. Future work can be pursued to estimate quantitative trends of the inverse-piezoelectricity induced instabilities and strategies to mitigate them. The fundamental nature of the phenomena, namely interaction of electric fields with piezoelectric coefficients, and insights from presented recovery trends suggest the inevitability of strain development in TMD devices during operation over their lifetime. However, the piezoelectricity-aware choice of architecture to account for electric fields existent in a device, coupled with strain-engineering through usage of capping layers and interface engineering can make these instabilities deterministic and tolerable for future TMD electronic devices.

In conclusion, despite their potential, the industrial adaptation of TMDs in scalable technologies has been constrained by unresolved characteristics instabilities and channel degradation, issues not commonly observed in conventional semiconductor materials. In this work, we identified a fundamental showstopper linked to an overlooked intrinsic property of TMDs, which, if unaddressed, could restrict their application to purely academic pursuits. By applying advanced spectroscopic techniques and time-resolved mapping, we investigated and uncovered how the intrinsic piezoelectric properties of TMDs introduce non-volatile strains under the applied electric field, revealing complex dynamics between these inverse piezoelectrically induced strains and the electrical properties of MoSe<sub>2</sub> FETs, providing crucial insights that could lead to fundamentally robust TMD-based technologies.

Systematic experimentation under both low and high electric fields from microseconds to 1000 s demonstrates significant alterations in device behaviors, such as current fluctuations, threshold voltage shifts, mobility changes, and increased contact resistance as a function of time. Our investigations demonstrated a unique strain disparity arising from the piezoelectric tensor's response to varying electric field vectors across different device regions. This resulted in the accumulation of tensile strain in the channel and compressive strain under the contacts, both found to be non-volatile. The non-volatile nature of strain and the strain mismatch at the channel-contact interface where tensile strain makes the TMDs in channel n-type and compressive



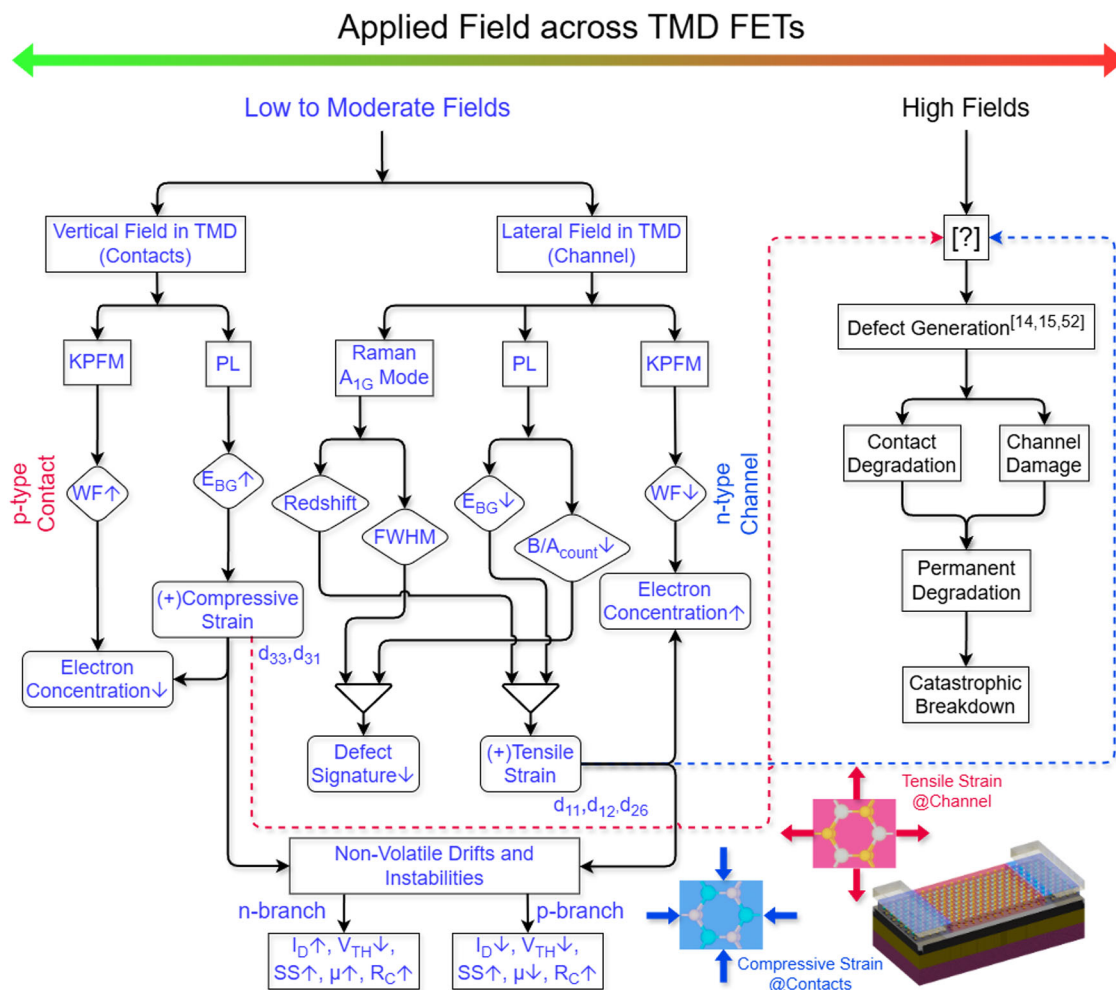


**Fig. 7 | Overview of the reported phenomena and correlation with previous reports at high operating fields<sup>14,15,76</sup>.** Inset device schematic depicting the overall effect seen in 2D TMD FET as compressive strain in contact region and tensile strain in channel region due to electrical operation.

strain makes it p-type under the contact. Such a work function mismatch in the device causes the device to exhibit electrical instabilities, irreversible changes post-electrical operation, governed by material reconfiguration under applied electric fields. Interestingly, while electrical operation seems to enhance TMD crystal ordering in the channel, potentially reducing defect-related issues, it simultaneously exacerbates failure mechanisms at the contacts, as evidenced by surface work function scans. Raman spectroscopy, photoluminescence (PL), and Kelvin probe force microscopy (KPFM) collectively confirmed the evolution of strain in the TMD due to electrical operation leading to localized non-volatile bandstructure fluctuations. The identified strain introduces drifts and instabilities in the properties of TMD in the devices, potentially revealing a fundamental parameter of inverse piezoelectricity in TMD devices (Fig. 7). Given the operational demands on short-channel TMD FETs, naturally resulting in high electric fields across the FETs, these findings, while discovering a fundamental showstopper, underscore the critical need to account for inverse piezoelectricity and associated strain alongside other well-studied factors such as interfaces, defects, and Fermi-level pinning in the development of robust TMD-based technologies.

## Methods

### Device fabrication

Back-gated multilayer MoSe<sub>2</sub> FETs were fabricated using standard mechanical exfoliation technique on 90 nm SiO<sub>2</sub> on p-type Si substrate and contacted using e-beam evaporated Palladium (Pd) contacts at ultra-high

vacuum to get ambipolar FETs<sup>73</sup>. The ambipolarity of devices was observed in  $I_D V_G$  with p-type conduction at negative  $V_{GS}$  and n-type conduction at positive  $V_{GS}$ . We chose to keep the channel length 3  $\mu\text{m}$  to facilitate reliable material characterization. Initial material characterization was done to choose the best performing few-layer FETs using  $\mu\text{Raman}$  and  $\mu\text{Photoluminescence}$  (PL) spectroscopy to confirm good thin channel material suitable for the study<sup>43,74</sup>. Electron potential map using Kelvin probe force microscopy (KPFM) technique for work function estimation showed MoSe<sub>2</sub> and Palladium electrode regions distinctly<sup>73,75</sup>. We further used CVD monolayer MoSe<sub>2</sub> and MoS<sub>2</sub> transferred on SiO<sub>2</sub> to perform required Raman, PL and KPFM scans to establish universal nature of phenomena.

### Electrical characterization

All electrical characterizations are performed in a state-of-the-art high vacuum probe station ( $\sim 2\text{e-}5$  torr) interfaced with a Keithley 4200A-SCS parameter analyzer. We used a measure-stress-measure scheme to electrically stress the devices where we measured the  $I_D V_G$  pre and post a stress where a device was subject to set of either low-field or high-field stresses. All sub-1s stresses were applied using the PMU (Pulse Measure Unit) unit and stresses more than 1 s were applied using the SMU (Source Measure Unit) unit. The PMU allowed for spot measurement of current and voltage and we sampled them at 70–80% window of pulses. Stress currents were captured with 1 s sampling when SMU was used. We kept the participation of oxide traps minimal by keeping the gate terminal floating during electrical stressing operation. This ensured that all the observed material changes were residual in nature and are due to the electrical stresses applied to the devices. The  $I_D V_G$

sweeps were performed in dual sweep mode with autoranging enabled for SMUs as it can reveal potential electrical traps due to adsorbates, and degradation. We did not observe a change in hysteresis due to the stressing performed in high vacuum condition<sup>27,28</sup>. Hence, single sweep data was taken for further parameter extraction and electrical analysis in the work.

A separate set of FETs were stressed for specific stressing time periods for material characterization. The channel and contacts were analyzed using various advanced spectroscopic techniques and the devices were compared to prestress characterizations to adjudge the drifts in material properties. This methodology allowed us to directly correlate the observed performance drifts with evolutionary changes in the material properties of the MoSe<sub>2</sub> channel and contacts, thereby elucidating the relationship between material transformations and alterations in device characteristics over time.

### Raman spectroscopy and photoluminescence

Raman spectroscopy and Photoluminescence measurements are done using a LABRam Horiba spectrometer with 1800 gratings/mm and 600 gratings/mm, respectively. We used a green laser (532 nm) with laser power kept below 100  $\mu$ W to ensure minimal laser induced structural damage during the optical explorations. The Raman spectra were obtained with the A<sub>1g</sub> peak of MoSe<sub>2</sub> and Si peak around  $\sim 520$  cm<sup>-1</sup>, all the spectra were corrected to have Si peak at 520.7 cm<sup>-1</sup>. We have used multilayered MoSe<sub>2</sub> which might have had different number of layers in devices, and to account for that, we compared pre and post stressing Raman and PL spectrum for individual devices to establish a more reliable trend of property drifts. Photoluminescence spectrum was baseline corrected and deconvoluted to separate out the A, B, and indirect excitonic transitions for further analysis.

### Kelvin Probe Force Microscopy (KPFM)

All KPFM measurements are done using Park NX-10 atomic force microscopy (AFM) system under ambient conditions. The AFM tips used to obtain potential maps are Cr-Pt coated ElectriMulti-75G with a tip radius of  $\sim 25$  nm. The tip potential was corrected against freshly cleaved surface of HOPG calibration sample. We used a single pass two-lockin AM-KPFM scanning technique in which the tip oscillates at its resonant frequency at set-point 10–12 nm away from surface. The first lockin obtains topography data to maintain tip-sample distance. A low frequency AC signal of 2 V at 17 kHz is applied to the tip via second lock-in which detects electrical signal from sample. The amplitude of signal obtained against applied AC bias at electrical resonance is used in the KPFM feedback to adjust the DC tip bias to nullify the contact potential difference between the tip and sample at each measurement point. The minute changes experienced in DC bias signal readout provided the surface potential image. The data is further corrected and processed in the XEI utility by Park Systems using a lowpass filter on acquired data and flattening the data across x and y-axis to account for signal drifts to obtain spatially resolved maps. The metal work function across the scans were corrected and equalized for fair comparison of TMD channel work function comparison.

### Data Availability

The data supporting the findings reported in this work are available from the corresponding authors upon reasonable request.

Received: 13 November 2024; Accepted: 23 April 2025;

Published online: 07 August 2025

### References

- Fiori, G. et al. Electronics based on two-dimensional materials. *Nat. Nanotechnol.* **9**, 768–779 (2014).
- Shrivastava, M. & Ramgopal Rao, V. A Roadmap for Disruptive Applications and Heterogeneous Integration Using Two-Dimensional Materials: State-of-the-Art and Technological Challenges. *Nano Lett.* **21**, 6359–6381 (2021).
- Illarionov, Y. Y., Knobloch, T. & Grasser, T. Crystalline insulators for scalable 2D nanoelectronics. *Solid State Electron* **185** (2021).
- Illarionov, Y. Y., Knobloch, T. & Grasser, T. Native high-k oxides for 2D transistors. *Nat. Electron* **3**, 442–443 (2020).
- Illarionov, Y. Y. et al. Improved hysteresis and reliability of MoS<sub>2</sub> transistors with high-quality CVD growth and Al<sub>2</sub>O<sub>3</sub> encapsulation. *IEEE Electron Device Lett.* **38**, 1763–1766 (2017).
- Illarionov, Y. Y. et al. The role of charge trapping in MoS<sub>2</sub>/SiO<sub>2</sub> and MoS<sub>2</sub>/hBN field-effect transistors. *2d Materials* **3** (2016).
- Illarionov, Y. Y. et al. Energetic mapping of oxide traps in MoS<sub>2</sub> field-effect transistors. *2d Materials* **4** (2017).
- Illarionov, Y. et al. Insulators for 2D nanoelectronics: the gap to bridge. *Nat. Commun.* **11**, 3385 (2020).
- Illarionov, Y. Y. et al. Reliability of scalable MoS<sub>2</sub> FETs with 2 nm crystalline CaF<sub>2</sub> insulators. *2d Mater.* **6**, 045004 (2019).
- Ma, X. et al. Defects induced charge trapping/detrapping and hysteresis phenomenon in MoS<sub>2</sub> field-effect transistors: mechanism revealed by anharmonic marcus charge transfer theory. *ACS Appl. Mater. Interfaces* **14**, 2185–2193 (2022).
- Knobloch, T. et al. A physical model for the hysteresis in MoS<sub>2</sub> transistors. *IEEE J. Electron Devices Soc.* **6**, 972–978 (2018).
- Ansh, A., Patbhaje, U., Kumar, J., Meersha, A. & Shrivastava, M. Origin of electrically induced defects in monolayer MoS<sub>2</sub> grown by chemical vapor deposition. *Commun. Mater.* **4**, 8 (2023).
- Shrivastava, M. & Ansh Superior resistance switching in monolayer MoS<sub>2</sub> channel-based gated binary resistive random-access memory via gate-bias dependence and a unique forming process. *J. Phys. D Appl. Phys.* **55** (2022).
- Ansh, Kumar, J., Sheoran, G. & Shrivastava, M. Electrothermal transport induced material reconfiguration and performance degradation of CVD-grown monolayer MoS<sub>2</sub> transistors. *NPJ 2D Mater. Appl.* **4**, 37 (2020).
- Ansh, A., Sheoran, G., Kumar, J. & Shrivastava, M. First insights into electro-thermal stress driven time-dependent permanent degradation failure of CVD monolayer MoS<sub>2</sub> channel. In: *Proc. IEEE International Reliability Physics Symposium (IRPS)* 1–4 (IEEE, 2020).
- Patbhaje, U., Verma, R., Kumar, J., Ansh & Shrivastava, M. Unveiling field driven performance unreliabilities governed by channel dynamics in MoSe<sub>2</sub>FETs. In: *Proc. IEEE International Reliability Physics Symposium Proceedings* vols 2023 (Institute of Electrical and Electronics Engineers Inc., 2023).
- Lin, Y. et al. Contact engineering for high-performance N-type 2D semiconductor transistors. In *Technical Digest - International Electron Devices Meeting, IEDM* vols 2021–December 37.2.1–37.2.4 (Institute of Electrical and Electronics Engineers Inc., 2021).
- Xiong, X. et al. Top-Gate CVD WSe<sub>2</sub>pFETs with record-high Id594  $\mu$ A/ $\mu$ m, Gm244  $\mu$ S/ $\mu$ m and WSe<sub>2</sub>/MoS<sub>2</sub>CFET based half-adder circuit using monolithic 3D integration. In: *Proc. Technical Digest - International Electron Devices Meeting, IEDM* vols 2022–December 2061–2064 (Institute of Electrical and Electronics Engineers Inc., 2022).
- Xiong, X. et al. Demonstration of Vertically-stacked CVD Monolayer Channels: MoS<sub>2</sub>Nanosheets GAA-FET with Ion>700:  $\mu$ A/ $\mu$ m and MoS<sub>2</sub>/WSe<sub>2</sub> CFET. In *Technical Digest - International Electron Devices Meeting, IEDM* vols 2021–December 7.5.1–7.5.4 (Institute of Electrical and Electronics Engineers Inc., 2021).
- Kumar, A. et al. Sub-200  $\Omega$ - $\mu$ m alloyed contacts to synthetic monolayer MoS<sub>2</sub>. In: *Proc. IEEE International Electron Devices Meeting (IEDM)* vols 2021–December 7.3.1–7.3.4 (IEEE, 2021).
- Chung, Y. Y. et al. First demonstration of GAA monolayer-MoS<sub>2</sub> nanosheet nFET with 410  $\mu$ A  $\mu$ m ID 1V VD at 40 nm gate length. In *Technical Digest - International Electron Devices Meeting, IEDM* vols 2022, 3451–3454 (Institute of Electrical and Electronics Engineers Inc., 2022).
- Dorow, C. J. et al. Gate length scaling beyond Si: mono-layer 2D channel FETs robust to short channel effects. In *Technical Digest - International Electron Devices Meeting, IEDM* vols 2022–December 751–754 (Institute of Electrical and Electronics Engineers Inc., 2022).
- Smets, Q. et al. Scaling of double-gated WS<sub>2</sub>FETs to sub-5nm physical gate length fabricated in a 300 mm FAB. In *Technical Digest - International*

- Electron Devices Meeting, IEDM* vols 2021–December 34.2.1–34.2.4 (Institute of Electrical and Electronics Engineers Inc., 2021).
24. Blonsky, M. N., Zhuang, H. L., Singh, A. K. & Hennig, R. G. Ab initio prediction of piezoelectricity in two-dimensional materials. *ACS Nano* **9**, 9885–9891 (2015).
25. Ng, L. R., Chen, G. F. & Lin, S. H. Generating large out-of-plane piezoelectric properties of atomically thin MoS<sub>2</sub> via defect engineering. *Phys. Chem. Chem. Phys.* **23**, 23945–23952 (2021).
26. Duerloo, K. A. N., Ong, M. T. & Reed, E. J. Intrinsic piezoelectricity in two-dimensional materials. *J. Phys. Chem. Lett.* **3**, 2871–2876 (2012).
27. Li, X. et al. Performance potential and limit of MoS<sub>2</sub> transistors. *Adv. Mater.* **27**, 1547–1552 (2015).
28. Ahn, J. H., Parkin, W. M., Naylor, C. H., Johnson, A. T. C. & Drndić, M. Ambient effects on electrical characteristics of CVD-grown monolayer MoS<sub>2</sub> field-effect transistors. *Sci. Rep.* **7** (2017).
29. Ali, M. S. M. M., Nguyen, H., Paci, J. T., Zhang, Y. & Espinosa, H. D. Thermomechanical properties of transition metal dichalcogenides predicted by a machine learning parameterized force field. *Nano Lett.* **24**, 8465–8471 (2024).
30. Hemanjaneyulu, K., Kumar, J. & Shrivastava, M. Gaps in the Y-function method for contact resistance extraction in 2D few-layer transition metal dichalcogenide back-gated FETs. *IEEE Electron Device Lett.* **43**, 635–638 (2022).
31. Hosseini, M., Elahi, M., Pourfath, M. & Esseni, D. Strain-induced modulation of electron mobility in single-layer transition metal dichalcogenides MX<sub>2</sub> (M = Mo, W; X = S, Se). *IEEE Trans. Electron Devices* **62**, 3192–3198 (2015).
32. Datye, I. M. et al. Strain-enhanced mobility of monolayer MoS<sub>2</sub>. *Nano Lett.* **22**, 8052–8059 (2022).
33. Postorino, S. et al. Strain-induced effects on the electronic properties of 2D materials. *Nanomater. Nanotechnol.* **10** (2020).
34. Doratotaj, D., Simpson, J. R. & Yan, J. A. Probing the uniaxial strains in MoS<sub>2</sub> using polarized Raman spectroscopy: a first-principles study. *Phys. Rev. B* **93**, 075401 (2016).
35. Kukucska, G. & Koltai, J. Theoretical investigation of strain and doping on the Raman spectra of Monolayer MoS<sub>2</sub>. *Phys. Status Solidi B Basic Res.* **254**, 1700184 (2017).
36. Zhao, S. et al. A Se vacancy induced localized Raman mode in two-dimensional MoSe<sub>2</sub> grown by CVD. <https://doi.org/10.48550/arXiv.1904.09789> (2019).
37. Saleta Reig, D. et al. Unraveling heat transport and dissipation in suspended MoSe<sub>2</sub> from bulk to monolayer. *Adv. Mater.* **34**, 2108352 (2022).
38. Chakraborty, B. et al. Symmetry-dependent phonon renormalization in monolayer MoS<sub>2</sub> transistor. *Phys. Rev. B Condens. Matter Mater. Phys.* **85**, 161403 (2012).
39. Zhang, Y. et al. Direct observation of the transition from indirect to direct bandgap in atomically thin epitaxial MoSe<sub>2</sub>. *Nat. Nanotechnol.* **9**, 111–115 (2014).
40. Cheng, X. et al. Using strain to alter the energy bands of the monolayer MoSe<sub>2</sub>: a systematic study covering both tensile and compressive states. *Appl. Surf. Sci.* **521**, 146398 (2020).
41. Deng, S., Li, L. & Li, M. Stability of direct band gap under mechanical strains for monolayer MoS<sub>2</sub>, MoSe<sub>2</sub>, WS<sub>2</sub> and WSe<sub>2</sub>. *Phys. E Low. Dimens. Syst. Nanostruct.* **101**, 44–49 (2018).
42. Ji, J. et al. Strain-modulated excitonic gaps in mono- and bi-layer MoSe<sub>2</sub>. *Chin. Phys. B* **25** (2016).
43. McCreary, K. M., Hanbicki, A. T., Sivaram, S. V. & Jonker, B. T. A- and B-exciton photoluminescence intensity ratio as a measure of sample quality for transition metal dichalcogenide monolayers. *APL Mater.* **6**, 11 (2018).
44. Zhang, Y. et al. Scaling law for strain dependence of Raman spectra in transition-metal dichalcogenides. *J. Raman Spectrosc.* **51**, 1353–1361 (2020).
45. Yang, Q., Xue, Y., Chen, H., Dou, X. & Sun, B. Photo-induced doping effect and dynamic process in monolayer MoSe<sub>2</sub>. *J. Semiconduct.* **41**, 082004 (2020).
46. Tonndorf, P. et al. Photoluminescence emission and Raman response of monolayer MoS<sub>2</sub>, MoSe<sub>2</sub>, and WSe<sub>2</sub>. *Opt. Express* **21**, 4908 (2013).
47. Island, J. O. et al. Precise and reversible band gap tuning in single-layer MoSe<sub>2</sub> by uniaxial strain. *Nanoscale* **8**, 2589–2593 (2016).
48. Conley, H. J. et al. Bandgap Engineering of Strained Monolayer and Bilayer MoS<sub>2</sub>. <https://doi.org/10.1021/nl4014748> (2013).
49. Rao, R. et al. Spectroscopic evaluation of charge-transfer doping and strain in graphene/ MoS<sub>2</sub> heterostructures. *Phys. Rev. B* **99**, 195401 (2019).
50. Chae, W. H., Cain, J. D., Hanson, E. D., Murthy, A. A. & Dravid, V. P. Substrate-induced strain and charge doping in CVD-grown monolayer MoS<sub>2</sub>. *Appl. Phys. Lett.* **111**, 14 (2017).
51. Zhang, B. et al. Effects of biaxial strain on phonon thermal transport properties of monolayer T'-WS<sub>2</sub>: a first-principles study. *J. Electron Mater.* **53**, 733–742 (2024).
52. Liu, J., Fang, M., Yang, E.-H. & Zhang, X. Reduction in thermal conductivity of monolayer MoS<sub>2</sub> by large mechanical strains for efficient thermal management. *Sci. Rep.* **15**, 1976 (2025).
53. Meng, X. et al. Thermal conductivity enhancement in MoS<sub>2</sub> under extreme strain. *Phys. Rev. Lett.* **122**, 155901 (2019).
54. Sohn, A. et al. Temperature-dependent piezotronic effect of MoS<sub>2</sub> monolayer. *Nano Energy* **58**, 811–816 (2019).
55. Patbhaje, U., Verma, R., Kumar, J., Dar, A. B. & Shrivastava, M. Decoupling current and voltage mediated breakdown mechanisms in CVD MoS<sub>2</sub>FETs. In: *Proc. IEEE International Reliability Physics Symposium*. <https://doi.org/10.1109/IRPS48228.2024.10529415> (Institute of Electrical and Electronics Engineers Inc., 2024).
56. Varghese, A. et al. Electrically controlled reversible strain modulation in MoS<sub>2</sub> field-effect transistors via an electro-mechanically coupled piezoelectric thin film (2023).
57. Shakya, J., Kumar, S., Kanjilal, D. & Mohanty, T. Work function modulation of molybdenum disulfide nanosheets by introducing systematic lattice strain. *Sci. Rep.* **7** (2017).
58. Grasser, T. et al. Analytic modeling of the bias temperature instability using capture/emission time maps. In: *Proc. International Electron Devices Meeting* 27.4.1–27.4.4 (IEEE, 2011).
59. Khan, M., Kedia, S. K., Mishra, A., Avasthi, D. K. & Tripathi, A. Investigation of the annealing temperature for few-layer MoS<sub>2</sub> and ion-beam induced athermal annealing/purification behaviour by in-situ XRD. *Appl. Surf. Sci.* **639**, 158106 (2023).
60. Illarionov, Y. Y. et al. Bias-temperature instability in single-layer graphene field-effect transistors. *Appl. Phys. Lett.* **105**, 14 (2014).
61. Doherty, J. L., Noyce, S. G., Cheng, Z., Abuzaid, H. & Franklin, A. D. Capping layers to improve the electrical stress stability of MoS<sub>2</sub> transistors. *ACS Appl. Mater. Interfaces* **12**, 35698–35706 (2020).
62. Peña, T. et al. Strain engineering 2D MoS<sub>2</sub> with thin film stress capping layers. *2d Materials* **8**, 045001 (2021).
63. Jaikissoon, M., Yang, J. A., Neilson, K. M., Pop, E. & Saraswat, K. C. Mobility enhancement of monolayer MoS<sub>2</sub> transistors using tensile-stressed silicon nitride capping layers. In *Device Research Conference - Conference Digest, DRC* vols 2022—June (Institute of Electrical and Electronics Engineers Inc., 2022).
64. Hoang, L. et al. Understanding the impact of contact-induced strain on the electrical performance of monolayer WS<sub>2</sub> transistors. *Nano Lett.* <https://doi.org/10.1021/acs.nanolett.4c02616> (2024).
65. Wang, Y. & Chhowalla, M. Making clean electrical contacts on 2D transition metal dichalcogenides. *Nat. Rev. Phys.* **4**, 101–112 (2021).
66. Park, J. et al. Statistical analysis of vertically stacked nanosheet complementary FET based on polycrystalline silicon with multiple grain boundaries. *Results Phys.* **63**, 107873 (2024).
67. Chen, M. L. et al. A FinFET with one atomic layer channel. *Nat. Commun.* **11**, 1205 (2020).



68. Kumar, J., Birla, S. & Agarwal, G. A review on effect of various high-k dielectric materials on the performance of FinFET device. In *Materials Today: Proceedings* vol. 79 297–302 (Elsevier Ltd, 2023).
69. Siddiqui, A., Khosa, R. Y. & Usman, M. High- k dielectrics for 4H-silicon carbide: present status and future perspectives. *J. Mater. Chem. C* **9**, 5055–5081 (2021).
70. Li, X. et al. Progress in photodetector devices utilizing transition metal dichalcogenides. *J. Mater. Chem. C* **12**, 1211–1232 (2024).
71. Ghosh, S. et al. Monolithic and heterogeneous three-dimensional integration of two-dimensional materials with high-density vias. *Nat. Electron* **7**, 892–903 (2024).
72. Pendurthi, R. et al. Monolithic three-dimensional integration of complementary two-dimensional field-effect transistors. *Nat. Nanotechnol.* **19**, 970–977 (2024).
73. Kumar, J. & Shrivastava, M. Role of chalcogen defect introducing metal-induced gap states and its implications for metal-TMDs' interface chemistry. *ACS Omega* **8**, 10176–10184 (2023).
74. Arora, A., Nogajewski, K., Molas, M., Koperski, M. & Potemski, M. Exciton band structure in layered MoSe<sub>2</sub> From a monolayer to the bulk limit. *Nanoscale* **7**, 20769–20775 (2015).
75. Gu, D., Dey, S. K. & Majhi, P. Effective work function of Pt, Pd, and Re on atomic layer deposited HfO<sub>2</sub>. *Appl. Phys. Lett.* **89**, (2006).
76. Albaridy, R. et al. Strain-induced sulfur vacancies in monolayer MoS<sub>2</sub>. *ACS Mater. Lett.* **5** 2584–2593 (2023).

## Acknowledgements

Authors would like to thank the 2D materials research group at MSDLab at IISc (Indian Institute of Science) Bangalore for fruitful discussions and fabrication facilities at CeNSE (Centre for Nano Science and Engineering), IISc Bangalore. Utpreksh Patbhaje and Rupali Verma would like to thank Swamajayanti Grant (No. SB/SJF/2021-22/16) and Prime Minister's Research Fellowship (PMRF) (No. PM/MHRD-20-17416) for funding the work.

## Author contributions

U.P., A.A., and M.S. conceived the idea and came up with experiments to validate the idea. U.P. fabricated the devices and performed the

experiments, processed data, analyzed the processed data, and wrote the paper. R.V., J.K., and M.S. contributed to analysis of the processed data. The final draft was prepared by U.P. with inputs from R.V., J.K., A.A., and M.S. M.S. supervised the work and provided necessary resources and tools to perform this study. All authors reviewed the final manuscript.

## Competing interests

The authors declare no competing interests.

## Additional information

**Supplementary information** The online version contains supplementary material available at <https://doi.org/10.1038/s41699-025-00564-2>.

**Correspondence** and requests for materials should be addressed to Utpreksh Patbhaje.

**Reprints and permissions information** is available at <http://www.nature.com/reprints>

**Publisher's note** Springer Nature remains neutral with regard to jurisdictional claims in published maps and institutional affiliations.

**Open Access** This article is licensed under a Creative Commons Attribution 4.0 International License, which permits use, sharing, adaptation, distribution and reproduction in any medium or format, as long as you give appropriate credit to the original author(s) and the source, provide a link to the Creative Commons licence, and indicate if changes were made. The images or other third party material in this article are included in the article's Creative Commons licence, unless indicated otherwise in a credit line to the material. If material is not included in the article's Creative Commons licence and your intended use is not permitted by statutory regulation or exceeds the permitted use, you will need to obtain permission directly from the copyright holder. To view a copy of this licence, visit <http://creativecommons.org/licenses/by/4.0/>.

© The Author(s) 2025